Laguerre-Gauss and Hermite-Gauss soft x-ray modes states generated using diffractive optics

J. C. T Lee,[1] S. Alexander,[2] S. D. Kevan,[1] S. Roy,[1,*] and B. McMorran[2,1]

[1] *Advanced Light Source, Lawrence Berkeley National Laboratory, Berkeley, CA 94720-8229, USA*
[2] *Department of Physics, University of Oregon, Eugene, OR 97403-1274, USA*

(Dated: May 24, 2018)

Light's capacity to carry angular momentum is integral to our knowledge of physics and ability to probe matter. In addition to spin, photons can occupy free-space orbital angular momentum (OAM) eigenstates.[1, 2] Visible light OAM is used in quantum information experiments, superresolution microscopy, optical tweezers, and angular momentum transfer to atoms in optical lattices.[3, 4] Soft x-ray OAM applications, slowed by the lack of suitable optics and rarity of coherent x-ray sources, could enable the direct alteration of atomic states through OAM exchange, and methods to study the electronic properties of quantum materials. We have made soft x-ray diffractive optics that generate single Laguerre-Gauss modes, observed carrying up to 30$\hbar$, or their superpositions. We also present Hermite-Gauss diffractive optics, and a soft x-ray OAM analyzer. This set of tools could enable both the manipulation and finer characterization of topologically complex or strongly correlated electronic matter, such as magnetic skyrmions or stripes in superconductors.

Efforts to generate and control x-ray and other short wavelength OAM beams is an active field of research. To create OAM in EUV ($\lambda \gtrsim 10$ nm), groups have used higher-order harmonic up-conversion with optical vortex laser pumps[5–7], off-axis synchrotron undulator radiation[8], and laser-seeded free electron laser techniques[9, 10]. (See Ref. [11], also.) In the hard x-ray regime ($\lambda \lesssim 0.1$ nm), phase singular optics, such as stepped phase plates[12] and spiral Fresnel zone plates[13] have been used.

Soft x-rays are ideally suited for probing the electronic structure and spin states of molecules and condensed matter. However, these wavelengths are too long to be compatible with hard x-ray optics, and too highly absorbing for use with visible/UV apparatus, making soft x-ray OAM difficult to generate. Binary amplitude diffractive optical elements[14, 15] have successfully been used to create soft x-ray beams characterized by single orbital angular momentum modes. In particular, Sakdinawat *et al.*[15] created and tested spiral zone plates for phase contrast enhancement in soft x-ray microscopy.

We chose to fabricate and test the performance of binary amplitude diffraction gratings that produce OAM-carrying Laguerre-Gauss (LG) TEM modes. LG modes are cylindrically-symmetric optical vortices characterized by a zero radial quantum number and an integer azimuthal quantum number ℓ. It has a doughnut-like transverse intensity profile, with a bright ring whose radius and OAM content are proportional to ℓ, and zero intensity at the center lying on the propagation axis. This dark center masks a singularity in the electric field phase, which evolves with the azimuthal angle as $\ell \times \phi$.

To imprint this phase singularity into an x-ray beam, we created fork dislocation gratings. In these gratings, half of the grating array contains ℓ additional slits compared to the other half. The ideal transmission function of such a fork grating is:

$$t_{0,\ell}(\rho, \phi) = (1 + \mathrm{sgn}[\sin(\frac{2\pi}{d}\rho\cos\phi + \ell\phi)])/2, \quad (1)$$

where d is the grating period far from the fork dislocation. In the far-field, the phase singularities appear at the diffraction maxima. Furthermore, the electric field around the m^{th} grating maximum varies as $\exp(i\ell m\phi)$. Thus, the OAM content of the LG modes is quantized and equal to the product of the number of defect slits in the fork grating and the index of the diffraction order: $(\ell \times m)\hbar$.

The binary amplitude fork gratings were made from gold substrates using focused ion beam milling. Soft x-ray diffraction measurements were performed at the Coherent X-ray Scattering Beamline (12.0.2.2) of the Advanced Light Source, Lawrence Berkeley National Laboratory. A high degree of transverse coherence is necessary for these experiments since the fork gratings, especially the extra slits, need to be coherently illuminated to imprint phase singularities into the x-ray beam. (See Methods for descriptions of both the diffraction and grating fabrication processes.)

Figure 1 shows a schematic of the coherent x-ray diffraction setup and, in Figs. 1(b) and 1(c), two vertically oriented fork gratings. While the gratings have the same nominal 400 nm periods, they have different ℓ values, *i.e.*, "topological charges" or numbers of extra slits. The grating in Fig. 1(b) has a topological charge of $\ell = 1$, while that in Fig. 1(c) has $\ell = 10$. As expected, the LG mode diameter and OAM content increases as a function of the diffraction order and ℓ-values: $|m| \times \ell$. For example, the outermost pair of LG modes ($|m| = 3$) in Fig. 1(b) contain $3\hbar$ units of OAM while those in Fig. 1(c) contain $30\hbar$, the highest we recorded. The

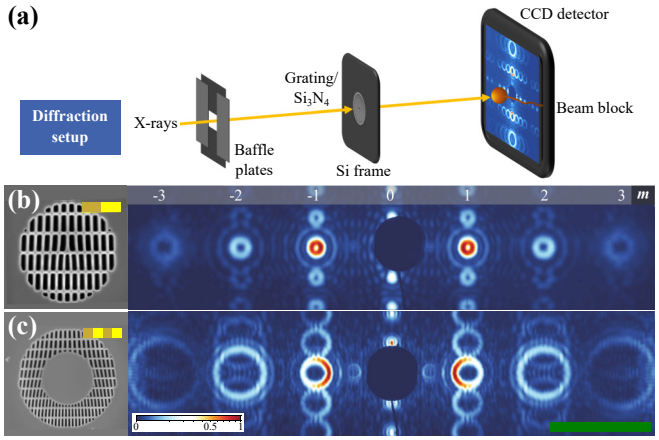

FIG. 1. Coherent soft x-ray diffraction: setup and fork gratings of topological charges $\ell = 1$ and $\ell = 10$. (a) Schematic of Beamline 12.0.2.2, Advanced Light Source, Lawrence Berkeley National Laboratory. (See Methods for experiment details.) Outlines of the baffle plates, Si frame, and beam block appear in our diffraction patterns. Left panels: SEM images of vertically oriented binary amplitude fork gratings with horizontal crossbar supports. (Scale bars are divided into 1 μm increments.) Right panels: coherent soft x-ray diffraction patterns (square root scale) with 10 mrad scale bar (green). (b) A $\ell = 1$ grating mounted on a circular mask of 5 μm diameter. LG modes are horizontally distributed, centered around fork grating maxima indexed by integer m, with OAM content equal to by $m\hbar$. LG mode diameters are proportional to OAM content. (c) A $\ell = 10$ grating mounted on a circular mask of 10 μm diameter. Even though the fork defect is unpatterned, LG modes carrying $10m\hbar$ appear. Vertically distributed copies of these LG modes form due to diffraction from the crossbars. Airy fringes around each LG mode are due to the sharp edges of the circular masks.

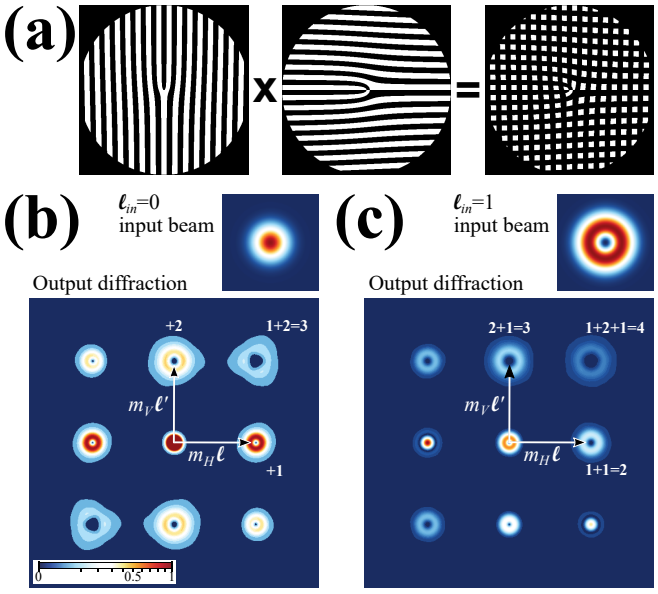

FIG. 2. OAM analyzer transmission function and simulated diffraction pattern. (a) The binary amplitude transmission function of an OAM analyzer is the product transmission function of two perpendicularly crossed fork grating functions: a $\ell = 1$ multiplier and $\ell' = 2$ multiplicand. (b) and (c) Simulated diffraction (square root scale) from a $\ell = 1$, $\ell' = 2$ OAM analyzer for $\ell_{in} = 0$ (part (b)) and $\ell_{in} = 1$ (part (c)) input beams (profiles in upper right, linear scale). The LG modes are distributed over a square lattice. The OAM content of a LG mode is determined by this sum: $(\ell_{in}+\ell\times m_H+\ell'\times m_V)\hbar$, where and m_H (m_V) are the horizontal (vertical) diffraction indices.

Airy fringes around each LG mode, particularly evident in the first order diffraction spots as rings around $|m| = 1$ LG modes in Fig. 1(b), are due to the sharp edges of the circular grating masks.

We used two methods to mechanically support the fragile fork gratings. As shown in Fig. 1(c), a large unpatterned section of Au substrate was left in the center to shorten the grating segments and reduce their chances of distorting or collapsing. We also added thin regularly spaced horizontal support crossbars.

The gratings produce well-defined LG modes regardless of the support method used. For example, fork gratings with unpatterned centers produce high quality LG modes, showing that the topological defect does not need to be illuminated. So long as enough grooves around the defect are illuminated, an optical vortex can be created. The supporting crossbars act like linear gratings, causing horizontally diffracted copies of the LG modes. Internal structure in the LG modes is a result of mode overlap.

We also made diffraction devices resembling two perpendicularly oriented fork gratings, which act as both OAM generators and OAM analyzers. The design and simulated performance of these analyzers are illustrated in Fig. 2. The transmission function of this analyzer can be described as the product of two fork grating transmission functions, with topological charges ℓ and ℓ', as given in Eq. 1: $t_{tot}(x, y) = t_{0,\ell}(x, y) \times t_{0,\ell'}(y, x)$. The example analyzer on the right side of Fig. 2(a) is produced by multiplying $\ell = 1$ and $\ell' = 2$ transmission functions. Coherent diffraction from this analyzer creates LG modes distributed over a square lattice. The horizontal and vertical positions of the lattice points are, respectively, indexed by integer m_H and m_V. Due to the addition and subtraction of OAM arising from constructive and destructive interference, the OAM of a LG mode at (m_H, m_V) depends on the topological charges of both the gratings and the input beam, ℓ_{in}:

$$\ell_{total} = (\ell_{in} + \ell \times m_H + \ell' \times m_V)\hbar. \qquad (2)$$

Simulated diffraction patterns (see Methods) for two different input beam cases, $\ell_{in} = 0$ and $\ell_{in} = 1$, are also shown in Fig. 2. For the $\ell_{in} = 0$ case (Fig. 2(b)) LG modes along the central rows and columns of the pattern are typical of separate $\ell = 1$ or $\ell' = 2$ gratings. The simulations show that the diffracted *intensity* pattern for a zero OAM input will possess inversion symmetry about

the central beam. (Note that the algebraic signs of the OAM carried by conjugate peaks are opposite.) This symmetry will be spoiled when incident soft x-rays carry OAM, illustrated by the $\ell_{in} = 1$ case (Fig. 2(c)). The magnitude and direction of this shift, according to Eq. 2, would reveal the OAM state of the input beam.

Compare the results of these simulations with coherent soft x-ray diffraction from two analyzers, performed with a nominally $\ell_{in} = 0$ input beam (the central radiation cone of an undulator carries no OAM) and whose diffractive outputs are shown in Fig. 3. Figure 3(a) shows diffraction from a $\ell = 1$ and $\ell' = 1$ analyzer while Fig. 3(b) has $\ell = 1$ and $\ell' = 2$. The inversion symmetry of Fig. 3(a) confirms that the incident beam has zero OAM. Furthermore, the good quantitative agreement between the relative intensities and diameters of the LG modes in Fig. 3(b) and Fig. 2(b) demonstrates the validity of our simulations.

Figure 3(a) is the simplest illustration of the OAM arithmetic enabled by these diffractive analyzers. The zero OAM input and unit topological charges of the analyzer's crossed fork gratings creates a pattern with progressively larger LG modes. Starting from the Gaussian peaks (red dots) on the upper left and lower right corners of the diffraction pattern, LG mode diameters increase in proportion to the $1\hbar$ change in OAM magnitude going from one diffraction order to the next along the rows and columns. Just as sending $+1\hbar$ incident x-rays caused the inversion center to shift to $(m_H, m_V) = (-1, 0)$ in Fig. 2(c), the Gaussian peaks in Fig. 3(a) would shift from $(\pm 1, \mp 1)$ to $(-1, 0)$ and $(0, -1)$, while $\ell = 1$ LG modes would occupy the old Gaussian peak positions. Alternatively, input of $-1\hbar$ x-rays would cause a shift to $(+1, 0)$ and $(0, +1)$. In each case, the sign and magnitude of the input OAM is revealed by the nature of the Gaussian peak shift, and the signature inversion symmetry found with a zero OAM input beam is lost.

We also made diffractive optics that create superpositions of LG modes. Figure 4(a), for example, displays a grating producing $\ell = 5$ LG modes with opposite magnetic numbers ℓ_z. The resulting interference produces flower petal-like fringes due to the dependence of the beam *amplitude* on the azimuthal angle around the peak positions.

To understand why the interference appears in the amplitude rather than the phase, consider the superposition of two general amplitude functions $f_1 = |f_1| \exp[i(\phi_r + \ell_1\phi)]$ and $f_2 = |f_2| \exp(i\ell_2\phi)$, where ϕ_r is an arbitrary phase offset, and ℓ_i is topological charge. Their superposition is $f_3 = f_1 + f_2 = |f_3| \exp[i\phi_3]$, where:

$$|f_3| = \sqrt{|f_1|^2 + |f_2|^2 + |f_1||f_2| \cos((\ell_1 - \ell_2)\phi + \phi_r)}$$
$$\phi_3 = ((\ell_1 + \ell_2)\phi + \phi_r)/2. \quad (3)$$

Equal amplitude gratings with opposite phase dependence, approximately true for the grating in Fig. 4(a), have $\ell_1 = -\ell_2$. The phase ($\phi_3 = \phi_r/2$) is a constant near the peak positions while the amplitude varies as a cosine of the azimuth, leading to the flower petal interference.

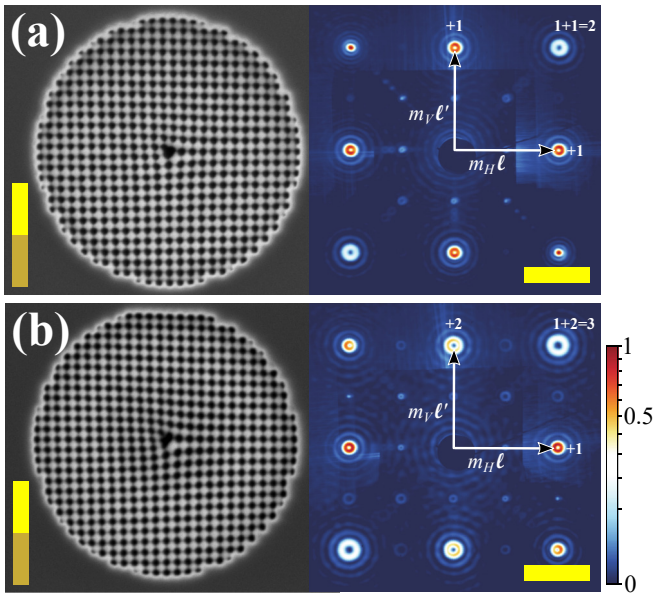

FIG. 3. OAM analyzers and their diffraction outputs. Left panels: SEM images of analyzers with 2 μm (real space, 1 μm increments). Right panels: coherent soft x-ray diffraction patterns (square root scale) with 10 mrad scale bar. (a) Diffraction from a $\ell = 1$, $\ell' = 1$ grating. Top left (bottom right) diffraction order is a single peak since $m_H = -m_V$. In the same column, bottom to top (top to bottom), OAM content increases by $1\hbar$ as indicated by rings of successively larger diameters. (b) Diffraction from a $\ell = 1$, $\ell' = 2$ grating, with similar trends in OAM content/LG mode diameter. Note that only LG modes with central singularities appear since $\ell \times m_H \neq -\ell' \times m_V$ for all diffraction orders reached by the CCD. Low intensity copies of the primary analyzer pattern occur due to higher x-ray harmonics in the input beam. Stray upstream x-rays and shadows of the supportive frame are also visible. Mask diameters: 5 μm, nominal grating periods: 200 nm Scale bars: 10 mrad (angle space), 2 μm (real space, 1 μm increments).

Intricate beam profiles, and the temperature gradients they cause through x-ray heating, could facilitate the nanoscale manipulation of magnetic vortices and skyrmions. Chiral skyrmion motion due to temperature gradients induced by a Gaussian electron beam has already been demonstrated in Cu_2OSeO_3.[16]

The x-ray LG vector potential can also enhance existing probes of nanoscale condensed matter properties. For example, electric quadrupole processes are predicted to strongly contribute to x-ray absorption OAM dichroism, which can be used to more clearly probe transition metal 3d states.[17] The resonant x-ray scattering intensity of magnetic vortices is predicted to strongly depend on the relative positions and topological charges of the vortex and beam.[18] This can be used in x-ray microscopy of magnetic vortices to reveal details of their spin textures.

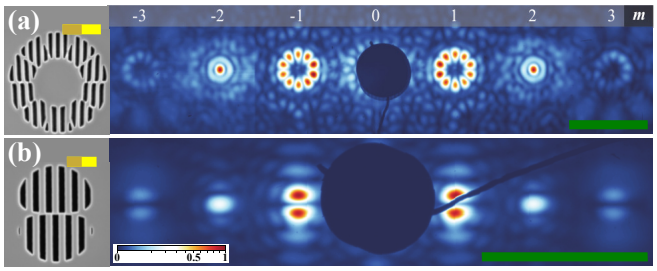

FIG. 4. Non-OAM carrying TEM modes: (a) superpositions of LG modes, (b) Hermite-Gauss (HG) modes. Left panels: SEM images of diffractive devices with 2 μm long scale bar (1 μm increments). Right panels: coherent soft x-ray diffraction patterns (square root scale) with 5 mrad scale bars. (a) LG superposition diffractive device creates LG modes occupying a superposition of $(\ell, \ell_z) = (5,\pm5)$ states, manifested by flower-like interference patterns centered at the diffraction maxima positions. Mask diameter: 5 μm, nominal grating period: 400 nm. (b) HG generating diffractive device creates $HG_{0,1}$ modes centered at the odd ordered diffraction positions, while single peaks appear at even orders. Mask diameter: 5 μm, nominal grating period: 200 nm.

The coupling of electronic and nuclear coordinates in the interaction Hamiltonian with a LG beam is projected to alter vibronic selection rules in molecules.[19]

Binary amplitude diffractive optics are not limited to LG solutions to Maxwell's equations. Figure 4(b) shows a diffractive device as well as soft x-ray Hermite-Gauss (HG) modes it created. Several diffractive HG optics in a highly coherent x-ray beam could be used in tandem to create higher order HG modes. While these carry no OAM, HG beams can be used to produce radial, azimuthal, or antisymmetric polarization profiles.[20] Radially polarized HG beams, focused by high numerical aperture lenses, can produce smaller focal spots than a linearly polarized Gaussian or LG beam. This can be used to significantly improve the spatial resolution of x-ray microscopy.

Modern nanotechnology allows fabrication of soft x-ray diffractive optics that made multiple types of beam-shaping and phase-structuring feasible, opening possibilities for powerful new x-ray spectroscopy and microscopy probes of materials. Diffraction limited x-ray sources with significantly increased coherent flux can make such techniques even more feasible and attractive.

METHODS

The diffraction measurement, diagrammed in Figure 1, was performed at the coherent x-ray Beamline (12.0.2.2) of the Advanced Light Source, Lawrence Berkeley National Laboratory. Beamline 12.0.2.2 produces soft x-rays with a high degree of transverse coherence compared to common synchrotron x-ray sources. The wavelength-dependent transverse coherence length of incident beam is 3.6-5.4 μm. [21] An Andor CCD detector recorded the diffraction (2048 $\times$ 2048 pixels, 13.5 μm pixel pitch), at a location 492 mm away from the sample. A beam block intercepts the grating zero-order. The beam spot is roughly elliptical ($\approx$ 20 μm $\times$ 200 μm). Soft x-ray diffraction patterns shown in this Letter were obtained with 2.480 nm (500 eV) x-rays, though patterns not shown here have been collected over a wavelength (photon energy) range of 1.240 nm (1000 eV) to 4.133 nm (300 eV).

The binary amplitude fork gratings were made using a Helios DB-FIB focused ion beam machine, located at Center for Advanced Materials Characterization in Oregon, University of Oregon, Eugene. Patterns generated using Eq. 1 were made using ion beam milling through 1 μm thick gold substrates, which were supported by 200 nm thick Si_3Ni_4 membranes mounted on Si frames. To accommodate the x-ray wavelength-dependent transverse coherence length, our grating patterns were limited to diameters of 5 or 10 μm, with 200 or 400 nm nominal grating periods.

OAM analyzer far-field diffraction was simulated by performing a Fourier transform of the product of the analyzer binary amplitude and incident beam amplitude functions. The diffracted intensities are calculated by obtaining the modulus squared of the Fourier transform.

AUTHOR CONTRIBUTIONS

B.M., S.R., and S.A. designed the experiment. S.A. fabricated the diffractive optics and performed SEM. J.C.TL. and S.A. performed the soft x-ray diffraction. J.C.TL, S.R., S.A., B.M., and S.D.K. wrote the manuscript.

This research used resources of the Advanced Light Source, which is a DOE Office of Science User Facility under contract no. DE-AC02-05CH11231. Work at the University of Oregon was supported by the U.S. Department of Energy, Office of Science, Basic Energy Sciences, under award no. DE-SC0010466.

* Corresponding author: sroy@lbl.gov

[1] L. Allen, M. W. Beijersbergen, R. J. C. Spreeuw, and J. P. Woerdman, Phys. Rev. A **45**, 8185 (1992).
[2] L. Allen, M. Padgett, and M. Babiker (Elsevier, 1999) pp. 291 – 372.
[3] S. Franke-Arnold, L. Allen, and M. Padgett, Laser & Photonics Reviews **2**, 299 (2008).
[4] S. W. Hell and J. Wichmann, Opt. Lett. **19**, 780 (1994).
[5] G. Gariepy, J. Leach, K. T. Kim, T. J. Hammond, E. Frumker, R. W. Boyd, and P. B. Corkum, Phys. Rev. Lett. **113**, 153901 (2014).

[6] R. Géneaux, A. Camper, T. Auguste, O. Gobert, J. Caillat, R. Taïeb, and T. Ruchon, Nature Communications **7**, 12583 EP (2016), article.

[7] F. Kong, C. Zhang, F. Bouchard, Z. Li, G. G. Brown, D. H. Ko, T. J. Hammond, L. Arissian, R. W. Boyd, E. Karimi, and P. B. Corkum, Nature Communications **8**, 14970 EP (2017), article.

[8] J. Bahrdt, K. Holldack, P. Kuske, R. Müller, M. Scheer, and P. Schmid, Phys. Rev. Lett. **111**, 034801 (2013).

[9] E. Hemsing, A. Knyazik, M. Dunning, D. Xiang, A. Marinelli, C. Hast, and J. B. Rosenzweig, Nat. Phys. **9**, 549 (2013).

[10] P. c. v. Rebernik Ribič, B. Rösner, D. Gauthier, E. Allaria, F. Döring, L. Foglia, L. Giannessi, N. Mahne, M. Manfredda, C. Masciovecchio, R. Mincigrucci, N. Mirian, E. Principi, E. Roussel, A. Simoncig, S. Spampinati, C. David, and G. De Ninno, Phys. Rev. X **7**, 031036 (2017).

[11] C. Hernndez-Garca, J. Vieira, J. T. Mendona, L. Rego, J. San Romn, L. Plaja, P. R. Ribic, D. Gauthier, and A. Picn, Photonics **4** (2017), 10.3390/photonics4020028.

[12] A. G. Peele, P. J. McMahon, D. Paterson, C. Q. Tran, A. P. Mancuso, K. A. Nugent, J. P. Hayes, E. Harvey, B. Lai, and I. McNulty, Opt. Lett. **27**, 1752 (2002).

[13] J. Vila-Comamala, A. Sakdinawat, and M. Guizar-Sicairos, Opt. Lett. **39**, 5281 (2014).

[14] D. Cojoc, B. Kaulich, A. Carpentiero, S. Cabrini, L. Businaro, and E. D. Fabrizio, Microelectronic Engineering **83**, 1360 (2006), micro- and Nano-Engineering MNE 2005.

[15] A. Sakdinawat and Y. Liu, Opt. Lett. **32**, 2635 (2007).

[16] M. Mochizuki, X. Z. Yu, S. Seki, N. Kanazawa, W. Koshibae, J. Zang, M. Mostovoy, Y. Tokura, and N. Nagaosa, Nature Materials **13**, 241 EP (2014).

[17] M. van Veenendaal and I. McNulty, Phys. Rev. Lett. **98**, 157401 (2007).

[18] M. van Veenendaal, Phys. Rev. B **92**, 245116 (2015).

[19] A. S. Rury, Phys. Rev. A **87**, 043408 (2013).

[20] Q. Zhan, Adv. Opt. Photon. **1**, 1 (2009).

[21] K. M. Rosfjord, Y. Liu, and D. T. Attwood, IEEE Journal of Selected Topics in Quantum Electronics **10**, 1405 (2004).